# Detecting 1/10th Scaled Structures in Dielectric Media Using Monostatic X-Band Radar Scattering Measurements

John D. Kekis†, Markus Testorf*, Michael A. Fiddy* and Robert H. Giles†

University of Massachusetts Lowell Research Foundation
600 Suffolk Street, Lowell, MA 01854

## ABSTRACT

Under the sponsorship of the U.S. Army's National Ground Intelligence Center (NGIC), researchers at U. Mass. Lowell's Submillimeter-Wave Technology Laboratory†(STL) and Center for Electromagnetic Materials and Optical Systems* (CEMOS) investigated the feasibility of detecting non-metallic structures embedded in various types of soil using a 1-GHz ground penetrating radar by establishing a 1/10th-scale laboratory environment with two spot-focussing X-band (10-GHz) lens antennae and an HP8510B Network Analyzer. Achieving similitude with the full-scale environment required fabricating replicas that were dimensional and dielectric scale-models of the non-metallic structures of interest (i.e. anti-personnel mines), as well as rocks, and soil with various levels of moisture content. The 1/10th-scale replicas were constructed from artificial dielectrics tailored such that the permittivity of the full-size objects at 10-GHz equaled the permittivity of the scale-models at 10.0-GHz. The monostatic X-band measurements were acquired in an anechoic environment, and digital images of the backscattered radar data from the 1/10th-scale composite scenes were processed using inverse synthetic aperture radar (ISAR) signal processing routines, and also PDFT superresolution imaging techniques. Based on the 1/10th-scale signature measurements performed, the feasibility of detecting a VS-50 anti-personnel mine buried in dry loam at a depth of 11.2mm was established. The full-scale radar cross-section of a VS-50 mine in this configuration was estimated to be -25 dBsm. Radar cross section values were not established for the structures embedded in the wet loam due to a change in the intensity scale (an inherent property of the superresolution algorithm), which changed for each image. However, the embedded objects were detected by the PDFT algorithm, showing promise for the future of this research.

**Keywords:** Scale Modeling, RCS Measurements, Compact Range, Ground Penetrating Radar, Monostatic Measurements, Superresolution, PDFT

## 1. INTRODUCTION

The Submillimeter-Wave Technology Laboratory (STL) has invested in two spot-focusing X-Band horn lens antennae with coaxial cables and X-Band waveguide in order to expand the range of frequencies available for free-space dielectric materials measurement, radar cross section, and rough surface scattering measurements. This X-band equipment, interfaced with an HP-8510B Network Analyzer and an IEEE interfaced computer, will constitute a laboratory radar system that will be capable of measuring the scattering parameters of various objects as a function of frequency. Further, in conjunction with a computer controlled rotary stage, it will be capable of acquiring monostatic and forward scattering data.

Utilizing the radar system at X-band frequencies, this research will investigate the feasibility of using a 1.0 GHz radar to detect and image non-metallic structures embedded in ground terrain over wet and dry soil conditions. Ground-penetrating radar (GPR) is a rapidly evolving technology for surface and subsurface investigations[1, 3]. To a GPR, these non-metallic structures will appear as dielectric discontinuities within the wet or dry loam. RF pulses have been used in radar and sonar for location and recognition of discontinuities in dielectric media[2]. Recognition was accomplished using correlation techniques. In this research, phase stable continuous-wave radar measurements will be performed over a continuous range of angles to allow the imaging of the dielectric discontinuities.

Remote sensing of the earth by electromagnetic radiation has been used in the past for many applications which are summarized in Tomiyasu[3] and Daniels[1]. These include radiometry, scatterometry, imaging, ocean surface dynamics & modeling, ocean surface temperature, sea salinity, sea ice detection, soil moisture determination, storm cell detection, atmospheric measurements, oil slick detection, crop identification, altimetry, microwave sensing in satellites, mapping the distribution of buried objects (drums, pipelines, etc.), defining the configuration of the water table and stratigraphic boundaries in the earth, and surveying waste-disposal sites. The closest application to this research is the mapping of buried objects within the earth.

With further research, these same techniques could be used in other frequency regimes for locating and recognizing tumors in the human body, and for other worthy causes.

Image Reconstruction from Incomplete Data, Michael A. Fiddy, Rick P. Millane, Editors,
Proceedings of SPIE Vol. 4123 (2000) © 2000 SPIE. · 0277-786X/00/$15.00

The potential scatterer is the Italian-made Valsella VS-50 Anti-personnel Scatter Drop Mine. The plastic shell of this mine has been tailored so that its properties almost match the terrain it is dropped in, making radar detection difficult. The dielectric properties (at 1 GHz) of rock, the plastic mine case, the TNT inside, as well as wet and dry loam were provided by Ulaby et. al., 1986.

For the acquisition of 1 GHz scaled signatures, dimensionally and electromagnetically scaled models of the mines, the loam (wet and dry), and the rocks in the ground will be fabricated. X-Band (8.2 – 12.4 GHz) radar will be used to provide scattering measurements within the laboratory. The antennae used are 16.62" in length (including lenses) and have a 12" aperture. At each antenna aperture, there are two plano-convex lenses attached to each other back-to-back. The inner lens serves to collimate the beam, and the outer lens focuses the beam at a distance of 35 in., with a 3dB beamwidth of 3.84" for the E-plane pattern, and a 3dB beamwidth of 4.45" for the H-plane pattern. The ratio of focal length to the lens diameter (F/d) for both antennae is equal to 1, and d = 12". The vertices of the lenses at the ends of the antennae are spaced 70" away from each other. Since each lens has a focal distance of 35", the focal planes of the two antennae coincide near the center of the optical table on which they are mounted, allowing the radiation from the two antennae to couple into each other. See Figure 2 for the experimental setup.

Since 10 GHz is the center of the X-band, the physical dimensions of the models will be scaled by $1/10^{th}$. The $1/10^{th}$ scale replicas will be fabricated with materials tailored such that the permittivity of the mines, rocks, loam, and TNT at 1 GHz (before scaling) equals the permittivity of the scaled models at 10 GHz. Various techniques for tailoring the properties of materials have been developed within the STL[5]. The theory behind building scale models of electromagnetic systems was established by George Sinclair in 1948[6]. The permittivity of the customized materials were measured using waveguide airline techniques with the HP-8510B network analyzer[7, 8, 9, 10, 11, 12, 13, 14, 15, 16], with estimated errors between 1% – 3%[16]. Each material's complex scattering parameters[17, 18] frequencies in the X-band were determined, and then their complex permittivity was extracted using the Newton-Raphson root-determination technique[19].

Results of monostatic scattering measurements and analysis over various angular ranges in the form of superresolved imagery will be presented in this report. Scaled models of the mines and rocks, as well as brass calibration spheres of various diameters will be imaged in free space by the X-Band compact radar range from the monostatic scattering they produce. They will be imaged with the PDFT superresolution imaging program while embedded within artificial ground plane models simulating soil at various moisture levels. Using the images of the calibration spheres as reference values, the $1/10^{th}$-scale and full-scale radar cross section of the embedded VS-50 mine will be determined.

For the most accurate free-space measurements possible, one must address certain issues associated with free-space work. The minimum transverse dimensions of the sample must be greater than three times the 3dB E-plane beamwidth of the antenna at the focal point or else diffraction from the edges of the sample will be reflected into the antennae, adding errors to the measurements[12]. Also, if focusing antennae are used, the material under test must be placed at the focal point of the beam while the radiation has a planar, far-field wavefront[12].

The anti-personnel mine under study is displayed in Figure 1. The dielectric properties of the plastic mine cases, the TNT inside the mines, the rock, and the wet and dry loam all at 1 GHz were provided by the army and are summarized in Tables 1200 and 1201 below. The materials from which these models will be fabricated, will be tailored such that their permittivity at 10 GHz equals the provided permittivity of the original materials in Table 2, 3, and 4 at 1 GHz.

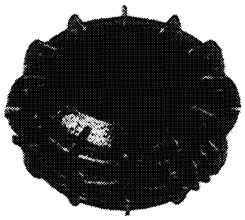

**Figure 1:** The Italian-Made Valsella VS-50
Anti-Personnel Scatter Drop Mine

The PDFT[20, 21, 22, 23, 24, 25] is a linear inverse scattering imaging algorithm, which uses the Born approximation of scattering, which is valid under the condition that the product of object size and permittivity contrast is small, which is true in the case of dielectric mine detection. The PDFT incorporates prior information about the object size and shape into the linear inverse scattering model, effectively providing a superresolved image.

| Valsella VS-50 Anti-Personnel Scatter Drop Mine | | |
|---|---|---|
| | ε' | ε'' |
| Plastic Casing | 3.9 | Small |
| TNT Inside | 2.9 | 0.05 |
| | | |
| Diameter (mm) | 90 | |
| Height (mm) | 32 | |
| Weight (g) | 185 | |

**Table 1:** Dielectric properties and dimensions of the VS-50 anti-personnel mine.

| | ε' | ε'' |
|---|---|---|
| Rock | 4.1 | small |
| Wet Loam | 8.1 | 1.4 |
| Dry Loam | 2.6 | 0.2 |

**Table2 :** Dielectric properties of rock, and wet and dry loam.

## 2. METHODOLOGY

An HP-8510B Network Analyzer was used as the transmitter / receiver, and was connected to the antennae via coaxial cable, waveguide, coax to waveguide adapters, and a rectangular to circular waveguide transitions. See Figure 2. The data acquisition program, written in LabVIEW, was designed to collect S11 data for any band of frequencies and incident angles.

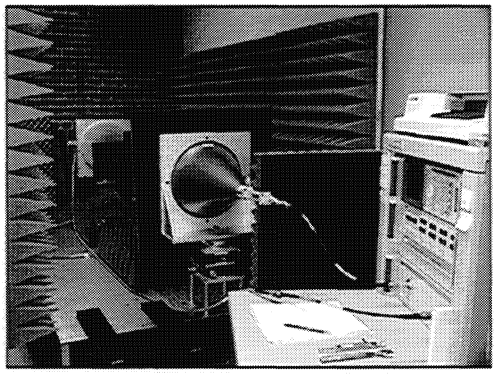

**Figure2:** X-Band compact radar range showing the HP-8510B Network Analyzer, two focusing antennae, a ground plane sample, and an anechoic chamber.

Retractable anechoic walls were built on the sides of the compact radar range to minimize contributions of reflected stray radiation from anything except the material under test. If undesirable effects still prevailed, time domain gating was utilized around the material being measured. A further reduction in contributions due to stray reflections is achieved mathematically using time domain gating. In order to perform an X-band free space calibration internal to the HP-8510B network analyzer, one must modify the X-band waveguide cal kit. Using the modified cal kit, a 2-port Thru Line Reflect (TRL) calibration can be performed. Two antennae are required for a free space calibration internal to the HP-8510B. The Thru measurement is one with no sample between the antennae. The Reflect measurement is one with a short (a large metal plate) located at the sample holder, at the mutual focal plane of the antennae. The traverse dimensions of the metal plate must be greater than three times the E-plane beamwidth at the focus to eliminate edge diffraction. The Line measurement is one with no sample between the antennae, but with the antennae separated by an extra $\lambda_o/4$ ($\lambda_o/8$ per antenna). These standards serve to specify the magnitude and phase up to the calibration reference planes, which are the two sides of the short used for the Reflect measurement. This calibration also eliminates any systematic error associated with the compact radar range. The length of the short along the axis parallel to the propagating beam serves as the "airline," or $L_{air}$, a parameter used in the Baker-Jarvis permittivity solving algorithm[7, 8, 9]. Any sample to be accurately measured (for any application) in free space should have a thickness smaller or equal to the airline length.

In order to match the permittivity of the materials listed in Tables 2 and 3, a Smooth-On® manufactured Rigid Urethane Casting Resin – Model#: C-1511, and also a Ciba Specialty Chemicals manufactured resin, TDT 205-3, – were used as binders. These are two-component liquid urethane systems, which cure to rigid plastics once mixed with an activator in a

1:1, or a 1:10 ratio by weight. The dielectric properties of the binders were tailored while still in liquid form by loading them with various percentages of strategically selected fillers, so that the permittivities of the resulting cured solids at 10 GHz equaled the permittivities of the materials in tables 2 and 3 at 1 GHz.
The fillers used were –325 mesh carbon graphite (C) powder (CERAC™ Inc., 99.5% pure, Item# G-1059), and or –325 mesh aluminum (Al) powder (Strem Chemicals, 99.7% pure, Item# 93-1344), and PTFE (Teflon) Powder with a particle mean diameter of 20μ (Goodfellow). For the purposes of this report, the definition for the loading amount of a binder will be referred to as the volumetric fill factor, whose definition is given in Equation 1. The amount of binder and filler used in mixing the samples were determined by volume using a Sartorius scale (0.001g-500g capability,) accompanied with knowledge of the density (see Table 3) for each filler and binder used.

| Density of Materials Used for Scale Models | |
|---|---|
| Name | Density, ρ [g/cm$^3$] |
| C-1511 Binder | 1.16 |
| TDT 205-3 Binder | 1.12 |
| Carbon Graphite | 1.7 |
| PTFE (Teflon) | 2.2 |
| Aluminum | 2.702 |

**Table 3:** Density of materials used for scaled models.

$$Vol.\,fill\,factor = \frac{\frac{m_f}{\rho_f}}{\frac{m_f}{\rho_f} + \frac{m_b}{\rho_b}}, \tag{1}$$

where, $m$ is the mass, $\rho$ is the density, and the subscripts $f$ and $b$ refer to *filler* and *binder* respectively.
A model ground plane thicker than its extinction coefficient was impractical to construct. To avoid constructive and destructive interference over the X-Band from the rear face of the ground plane, wedged anechoic modeled after FIRAM[26] fabricated from the same material as the ground plane using a mold was impedance matched to the back of the ground plane in order to dampen the wave so that the reflected field from the rear face of the ground plane would be very weak.

| Monostatic Measurements Performed on the Ground Plane Simulating Dry Loam | | | | | |
|---|---|---|---|---|---|
| **NAME / DATE** | **Left Plug** | **Right Plug** | **Separation** | **Angular Range (°)** | **Resolution (°)** |
| X-DGP-M1 | Empty | Empty | N/A | -50 to 50 | 2 |
| X-DGP-M2 | Brass Sphere (d = 0.375") | Brass Sphere (d = 0.625") | 0.0293 m | -32 to 32 | 2 |
| X-DGP-M3 | Brass Sphere (d = 0.375") | VS-50 Mine | 0.0333 m | 0 to 63 | 2 |
| X-DGP-M4 | Brass Sphere (d = 0.375") | Scaled Rock | 0.0315 m | 0 to -63 | 2 |

**Table 4:** Monostatic measurements performed on the ground plane simulating dry loam.

| Monostatic Measurements Performed on the Ground Plane Simulating Wet Loam | | | | | |
|---|---|---|---|---|---|
| **NAME / DATE** | **Left Plug** | **Right Plug** | **Separation** | **Angular Range (°)** | **Resolution (°)** |
| X-WGP1-M4 | Brass Sphere (d = 0.375") | Brass Sphere (d = 0.375") | 1.65" | 0 to 63 | 1 |
| X-WGP1-M5 | Brass Sphere (d = 0.375") | Brass Sphere (d = 0.375") | 1.65" | -32 to 32 | 1 |
| X-WGP1-M6 | Empty | Empty | N/A | 0 to 63 | 1 |
| X-WGP1-M7 | Brass Sphere (d = 0.375") | Brass Sphere (d = 0.375") | 1.65" | 0 to -63 | 1 |
| X-WGP1-M8 | Brass Sphere (d = 0.375") | VS-50 Mine | 1.65" | -63 to 63 | 1 |
| X-WGP1-M9 | VS-50 Mine | VS-50 Mine | 1.65" | -63 to 63 | 1 |
| X-WGP1-M10 | Empty | Empty | N/A | -63 to 63 | 1 |

**Table 5:** Monostatic measurements performed on the ground plane simulating wet loam.

| Properties of Various Full-Scale and 10th Scale Anti-Personnel Mines, Ground Planes, and Rocks | | | | | |
|---|---|---|---|---|---|
| | FULL SCALE @ 1- GHz | | | 10th SCALE @ 10- GHz | |
| | ε' | ε'' | %ff in C-1511 or 205-3 | ε' | ε'' |
| **VS-50 Plastic Shell** | 3.9 | | **3.299%** C in C-1511 | 3.97 | 0.14 |
| **TNT Inside** | 2.9 | 0.05 | **0.326%** C in C-1511 | 2.92 | 0.04 |
| **Wet Loam (1)** | 8.1 | 1.4 | **6.436%ff 5.3**C:**1.1**Al in C-1511 | 8.65 | 0.35 |
| **Dry Loam** | 2.6 | 0.2 | **0%** Loading; TDT 205-3 | 2.79 | 0.1 |
| **Rock** | 4.1 | | **3.299%** C in C-1511 | 3.97 | 0.14 |
| **Wet Loam (2)** | 8.1 | 1.4 | **89.6**C-1511:**5.8**C:**3.6**aPTFE:**0.92**Al | 7.04 | 0.322 |

**Table 6:** Summary of the dielectric properties of the full-scale structures of interest, as well as for the materials that were chosen to simulate them.

## 3. RESULTS

### 3.1 Materials

In order to determine the appropriate materials with which to construct the scaled models required for this research, the dielectric properties of many customized materials were measured. Of the many materials tested, the closest complex permittivity match for each full-scale scatterer was chosen and compiled onto Table 6. This table contains both descriptions and dielectric properties of the full-scale structures, as well as details pertaining to the corresponding materials chosen to construct the $1/10^{th}$-scale models. The composition of the materials were described as volumetric ratios. For example, if a material were labeled "90 C-1511 : 6 C : 5 PTFE," this material was composed of 90%C-1511 Resin Binder, 6% Carbon Graphite, and 5% Teflon by volume.

### 3.2 Ground Plane

In order to build a virtually infinitely deep ground plane, the extinction depths of the materials chosen to simulate wet and dry loam were determined, and compared with those of their full scale counterparts. Table 7 contains extinction depths for full scale wet and dry loam, and for materials which best match their dielectric properties. There are three $1/10^{th}$-scale simulations given for wet loam in Table 7. For strategic purposes, only the wet loam simulation 1 material was used in constructing an artificial wet loam ground plane. It was determined that using a flat-plate ground plane (without an anechoic attachment) caused relatively strong reflections from the back face of the ground plane that drowned out the weak backscatter of the mines. In comparing the normal incidence reflection of the ground plane with and without the anechoic attachment, a factor of 3.7 reduction in the unwanted flat-plate interference effects was observed when using the anechoic attachment.

| Extinction Depth for Ground Planes | (3 $\delta$) |
|---|---|
| **Dry Loam Full Scale (1GHz); $\varepsilon$ = (2.6, 0.2)** | **88.3"; 10th Scaled: 8.83"** |
| **10th Scale Dry Loam Simulation 1; $\varepsilon$ = (5.5, 0.26)** | 9.87"@10.3 GHz |
| **10th Scale Dry Loam Simulation 2; $\varepsilon$ = (2.79, 0.095)** | 19.24" @10.3 GHz |
| **Wet Loam Full Scale (1GHz); $\varepsilon$ = (8.1, 1.4)** | **22.3"; 10th Scaled: 2.23"** |
| **10th Scale Wet Loam Simulation 1; $\varepsilon$ = (8.65, 0.35)** | 9.197" @10.3 GHz |
| **10th Scale Wet Loam Simulation 2; $\varepsilon$ = (5.63, 0.282)** | 9.21" @10.3 GHz |
| **10th Scale Wet Loam Simulation 3; $\varepsilon$ = (6.88, 0.45)** | 6.38" @10.3 GHz |

**Table 7:** Extinction depths of full-scale wet and dry loam, and of certain tailored materials from Table 8 that best match their dielectric properties.

### 3.3 Dry Loam Results

Superresolved PDFT images displaying the results of the monostatic experiments involving dry loam model are shown in Figures 3 to 6. Each image shown is that of the dry ground plane with empty plugs, digitally subtracted from the ground plane with embedded objects. The units of the $x$ and $y$ axes of each image are in meters. The $z$-axis (the color axis) represents the magnitude of the intensity of the backscatter from the various embedded structures. Every object is buried 1.12mm beneath the scaled ground plane modeling a full-scale depth of 11.2mm. Figure 3 is a superresolved image of measurement X-DGP-M1 subtracted from the image of measurement X-DGP-M2 (small sphere on left, large sphere on right). See Table 7 for detailed experimental parameters. Figure 4 is a superresolved image of measurement X-DGP-M1 subtracted from the image of measurement X-DGP-M3 (small sphere on left, VS-50 Mine on right). See Table 4 for detailed experimental parameters. Figure 5 is a superresolved image of measurement X-DGP-M1 subtracted from the image of measurement X-DGP-M4 (small sphere on left, model rock on right). See Table 4 for experimental parameters. The rock did not appear in this image. Figure 6 is a repeat image of Figure 5, but was reconstructed using different parameters for the PDFT imaging algorithm so that the rock may be successfully imaged. Table 8 contains a summary of the results for $1/10^{th}$-scale and full-scale radar cross sections of objects embedded in dry loam. It also contains the radar cross section of the VS-50 mine ($\sigma_{predicted}$) predicted by a rough theoretical model developed to examine the credibility of the experiment and its analysis.

| 1/10th-Scale and Full-Scale Theoretical, Measured, and Predicted Radar Cross Sections of Objects Embedded 1.12mm Beneath Dry Loam for 1/10th-Scale, and 11.2mm Beneath Dry Loam for Full-Scale | | | | |
|---|---|---|---|---|
| | [$m^2$] | [dBsm] | [$m^2$] | [dBsm] |
| **Scatterer** | **$\sigma_{theory}$ (1/10th-Scale)** | | **$\sigma_{theory}$ (Full-Scale)** | |
| 0.625" Sphere | 1.979E-04 | -37.035 | N/A | N/A |
| 0.375" Sphere | 7.126E-05 | -41.472 | N/A | N/A |
| | **$\sigma_{measured}$ (1/10th-Scale)** | | **$\sigma_{measured}$ (Full-Scale)** | |
| VS-50 Mine | 3.001E-05 | -45.228 | 3.001E-03 | -25.228 |
| | **$\sigma_{predicted}$ (1/10th-Scale)** | | **$\sigma_{predicted}$ (Full-Scale)** | |
| VS-50 Mine | 3.428E-05 | -44.649 | 3.428E-03 | -24.649 |

**Table 8:** 1/10th-Scale and Full-Scale Radar Cross Sections of Scatterers Embedded in Dry Loam

### 3.4 Wet Loam Results

Superresolved PDFT images displaying the results of the monostatic measurements involving the wet loam model are shown in Figures 7 and 8. Each image shown is that of the wet ground plane with empty plugs, digitally subtracted from the ground plane with embedded structures. Figure 7 is a superresolved image of measurement X-WGP1-M10 subtracted from the image of measurement X-WGP1-M8 (small sphere on left, VS-50 mine on right). See Table 5 for detailed experimental parameters. Figure 8 is a superresolved image of measurement X-WGP1-M10 subtracted from the image of measurement X-WGP1-M9 (two embedded VS-50 mines). See Table 5 for detailed experimental parameters.

## 4. DISCUSSION

### 4.1 Materials

A summary of the materials used to model the required full-scale structures is given in Table 6. The plastic shell of the VS-50 mine was reported as a low-loss structure, so the imaginary component of its permittivity was assumed to be negligible. The average percent difference between the real permittivity between full-scale and 1/10th scale objects was 4% (excluding the wet loam simulation 2, which was not used in experiments). Individually, the real and imaginary parts of the permittivity were rather easy to match. Scaling materials to simultaneously match both the real and imaginary permittivity components for the TNT was also easy. The difficulty arose when attempting to simultaneously match the real and imaginary permittivity components for wet and dry loam. Since loam usually has some moisture content, its ratio of real to imaginary permittivity is rather low relative to other materials due to the fact that water is highly attenuating at radar frequencies. In other words, it has an unusually high imaginary permittivity compared to materials tested with the same value for the real permittivity. Materials experiments showed that real permittivity increases very quickly as the fill factor of aluminum powder increases in C-1511. They also showed that the real permittivity increase using carbon graphite powder as the filler is much less rapid. From these results, it is apparent that aluminum powder should not be used to model wet or dry loam, since the required permittivity has low real and high imaginary components.

In order to match the properties of wet and dry loam, a method of lowering the real permittivity, while increasing the imaginary part was required. Many popular anechoic materials are constructed using a foamy material with many air pockets, but with conductive particles surrounding the hollow regions (such as the anechoic used to construct the anechoic chamber in Figure 2). The theory being that the air pockets would keep the real permittivity low, and embedded conductive particles would increase the imaginary permittivity. Since the technology of introducing air-bubbles homogeneously within the test materials was not practical with in-house resources, a low loss material, Teflon powder (PTFE) was used instead. Experiments[27] showed that as the fill factor of Teflon was increased in C-1511, the real permittivity decreased, while the imaginary permittivity increased Performing the same experiment using TDT 205-3 as a binder, as the fill factor of Teflon increased, both the real and imaginary components of the permittivity decreased. The reason for this is that the binder TDT 205-3 has a naturally high imaginary permittivity component compared to its real part. C-1511 does not have this useful feature. The properties of C-1511 with no loading are $\varepsilon = 2.86 - i\ 0.03$, while for TDT 205-3 with no loading, the permittivity is $\varepsilon = 2.79 - i\ 0.1$ . It is clear that both wet and dry loam should be modeled using a binder with a naturally high

imaginary permittivity, such as TDT 205-3. For matching plastics, it is wise to start off with a binder that has a low imaginary permittivity, such as C-1511.

### 4.2 Ground Plane

Experiments[27] proved the usefulness of an anechoic attachment on a ground plane. It was shown that interference effects from the back surface of the ground plane were reduced by a factor of 3.7. Using the range cross-range imaging, the beneficial effects of the anechoic attachment were observed. Images of the ground plane without the anechoic attachment appeared thicker in the range direction than they should theoretically be according to range resolution calculations ($\Delta R_{Range}$ = 5.62"), which state that any object less than 5.62" long in the range direction should occupy only one range bin. Such poor resolution is inherent to imaging programs that do not use superresolution. The multiple reflections from the back face of the ground plane did in fact drown out scattering from two embedded metallic spheres, which means that they definitely would have enveloped the signal from the weakly scattering mines.

### 4.3 Dry Ground Plane Simulation and Radar Cross Section Calculations of the Embedded VS-50 Mine

The separation distance of the images corresponding to the embedded structures for the dry ground plane in Figures 3 - 6, matched precisely with the actual object separations given in Table 4.

In order to verify the relative cross section between two objects accurately, and to eventually be able to determine the full-scale cross section of the mines, one must have at least two calibration objects with known cross sections. For this purpose, two metallic calibration spheres with differing diameters have been imaged 1.12mm below the dry ground plane simulation. The smaller sphere had a diameter of 0.375", and the larger sphere had a diameter of 0.625". The theoretical free-space cross sections of the metallic spheres were determined using Equation 2, an equation provided in any Radar handbook. The only twist to the formula is the use of a scale factor, *S*, which is equal to 1 for $1/10^{th}$-scale measurements, and is set equal to 10 to determine the full-scale cross section of any $1/10^{th}$ scaled object.

$$\sigma_{Sphere} = \pi(Sr)^2, \tag{2}$$

where, $\sigma$ is the cross section of a sphere in [$m^2$], $r$ is the radius of the sphere, and $S$ is a scale factor ($S$ = 1 for $1/10^{th}$-scaled objects, and S = 10 for full-scale objects). It is useful to convert any cross section into decibel units, with the standard being a metal plate having an area of $1m^2$. Any cross section given in units of [$m^2$] may be converted into units of [dBsm] (or [$dBm^2$]) by using Equation 3. All final cross section results will be given in units of dBsm.

$$\sigma[dBsm] = 10 \cdot \log\left(\sigma\left[m^2\right]\right), \tag{3}$$

The scale factor in Equation 2 was included, since everything was scaled by $1/10^{th}$, and will eventually be converted back to full-scale. If $S$ is set equal to 10, the resulting cross section will accurately predict a full-scale cross section.

The ratio of the cross sections of two differently sized spheres in free space should be equal to the ratio of the cross sections of the two spheres embedded in the loam. This method is used to verify the accuracy of the images produced, and also to obtain the cross section of a test object (e.g. a VS-50 mine).

Using Equations 2 and 3, the theoretical cross section of the large sphere is:

$$\begin{aligned} \sigma_{LS} &= \pi(1 \cdot 0.0079375m)^2 = 1.979 \times 10^{-4} m^2 \\ \sigma_{LSdB} &= 10 \cdot \log(\sigma_{LS}) = -37.035\, dBsm \end{aligned}, \tag{4}$$

and the theoretical radar cross section of the small sphere is:

$$\begin{aligned} \sigma_{SS} &= \pi(1 \cdot 0.0047625m)^2 = 7.126 \times 10^{-5} m^2 \\ \sigma_{SSdB} &= 10 \cdot \log(\sigma_{SS}) = -41.472\, dBsm \end{aligned}, \tag{5}$$

The ratio between the theoretical radar cross sections of the two spheres is:

$$\frac{\sigma_{LS}}{\sigma_{SS}} = \frac{1.979 \times 10^{-4}}{7.126 \times 10^{-5}} = 2.78, \tag{6}$$

Examining Figures 3 and 4, it is apparent that the peak intensity of the large sphere is $I_{LS}$ = 4.10, the peak intensity of the small sphere is $I_{ss}$ = 1.90, and the peak intensity of the VS-50 mine is $I_{mine}$ = 0.80 . It can be seen that the magnitude axis (the color scale) in Figures 3, 4, and 5 are the same. The small sphere is present in each image, and its intensity is always $I_{ss}$=1.90. Since the rock was not visible in Figure 5, the PDFT parameters were altered to provide extra superresolution at the expense of more artifacts (Figure 6). Unfortunately, that altered the magnitude scale. Therefore, the radar cross section of this particular rock in Figure 6 cannot be inferenced using the relative intensity of the images of the calibration spheres.

The ratio between the measured intensities of the large sphere to the small sphere is:

$$\frac{I_{LS}}{I_{SS}} = \frac{4.1}{1.9} = 2.2, \tag{7}$$

which is close to the theoretical value given in Equation 6.

The measured $1/10^{th}$-scale radar cross section of the VS-50 mine referenced to the relative theoretical cross section of the small sphere is:

$$\sigma_{VS50} = \sigma_{SSdB} + 10 \cdot \log\left(\frac{I_{mine}}{I_{SS}}\right) = -45.228, \tag{8}$$

Since the $1/10^{th}$-scaled radar cross section of the VS-50 mine ($\sigma_{VS50}$) was measured to be -45.228 dBsm using equations 2 and 3 with S = 10, the full-scale radar cross section ($\sigma_{VS50\,fs}$) of a real VS-50 mine buried 1.12 mm beneath dry loam is predicted to have a value of:

$$\sigma_{VS50\,fs} = 10 \cdot \log\left[\pi(10 \cdot 0.0047625m)^2\right] + 10 \cdot \log\left(\frac{I_{mine}}{I_{SS}}\right) = -25.228\,dBsm, \tag{9}$$

### 4.4 Wet Ground Plane Simulation

The material from Table 6 chosen to represent wet loam for this research was not necessarily the material which most closely matched the given full-scale permittivity values. It was difficult at first to match both the real and imaginary parts of wet loam, since the imaginary permittivity of the measured materials was never high enough relative to the real component. It was decided to simulate wet loam by using a model whose real permittivity was a close match to the provided full-scale value. This model was the "$10^{th}$ Scale Wet Loam Simulation 1" from Table 6. Its imaginary permittivity was only 0.35 compared to the provided full-scale wet loam value of 1.4, but the real parts matched rather well. Since the real part of the permittivity contributes most to the magnitude of the reflection of a material, and the imaginary part contributes more to the attenuation, the simulation provided a decent match. Since the real permittivity matched well, but the imaginary permittivity fell short of the actual values, imaging embedded objects would be slightly easier than if both components of the permittivity were matched. Therefore, if embedded objects could not be imaged using this wet loam simulation, then it is highly unlikely that it would be possible to image the objects in full-scale wet loam. The other wet loam simulations in Table 6, simulations 2 and 3, were created late in the experiment. These materials were tailored using Teflon, as well as carbon graphite and aluminum. The Teflon allowed a closer match to the provided full-scale values. If TDT-205-3 were used instead of C-1511, the match would be even closer, since TDT 205-3 has a much higher natural imaginary permittivity than that of the C-1511 binder.

Figure 7 is a wet loam image of the small sphere and the VS-50 mine, and Figure 8 is a wet loam image of two VS-50 mines side by side. The separation distance of the images corresponding to the embedded structures for the wet ground plane in Figures 7 and 8, matched the actual object separations given in Table 5. However, the magnitude (color) scales for the two images were not consistent with one another. To illustrate the problem, the intensity of a mine in Figure 8 is greater than the intensity of the small sphere in Figure 7. Therefore, radar cross section information cannot be inferenced from the wet ground plane data.

The PDFT reconstructions did not use all of the data obtained by the monostatic measurements. Even though the measurements were obtained using resolutions as high as 1°, with complex S11 values for 201 equally spaced frequency values, the PDFT utilized data in resolutions of 5°, with 101 S11 values over the X-band due to the large amount of computer memory required to run the program.

## 5. CONCLUSION

Methods for accurately tailoring materials for use in scaled electromagnetic systems have been established, and a functional radar range was built. Experiments conducted using this range showed that non-metallic mine detection under simplified conditions is possible, but must be further developed for full-scale use. It was also shown that it is easier to detect these anti-personnel mines in dry loam than in wet loam. The PDFT algorithm worked without any trouble for the dry loam images with embedded structures of reasonable cross section. However, slight changes to the program's parameters had to be implemented when reconstructing wet loam images, and dry loam images with an embedded rock. The distance between scatterers was portrayed with extreme accuracy using PDFT imagery. The full-scale radar cross section of a VS-50 mine embedded beneath 11.2mm of dry loam was estimated to be –25 dBsm based on the $1/10^{th}$ scale signature measurements performed. Radar cross section values were not established for the structures embedded in the wet loam due to the intensity

scale, which changed for each wet loam image. However, the embedded objects, which were detected by the PDFT algorithm, show promise for future work.

## 6. RECOMMENDATIONS

Upgrading the compact radar range to obtain fully-polarimetric measurements would result in higher quality image reconstructions, increasing the chances of successfully detecting embedded structures in both wet and dry loam without resorting to image subtraction, as was done with this thesis. The upgrade to the range would involve the development of a calibration sequence external to the HP8510B network analyzer, and the introduction of new hardware, such as a beamsplitter and an amplifier, since the system could easily become signal limited due to the fact that the current maximum power output of the network analyzer is 20dBm. Polarimetric signature content also provides amplitude variability between the H and V electric field, which can often be attributed to the symmetry of scattering structures. The PDFT algorithm should also be further developed by exploiting the measurement techniques established with this research for obtaining high quality, repeatable data on scaled ground planes that can be modeled more realistically as the program improves by the addition of rough surfaces, vegetation modeling, etc.
For color images and detailed tables and figures that prove certain statements made in this article, see Kekis[27].

## 7. ACKNOWLEDGEMENTS

We would like to thank the students and staff of the Submillimeter-Wave Technology Laboratory, and especially Dr. Robert Giles, for their support of this research. This project was funded by the National Ground Intelligence Center.

## 8. REFERENCES

1. Daniels, J. J., Technical Review: ground penetrating radar. In Proc. (2nd) Symposium on the Application to Engineering and Environmental Problems, Soc. Engineering and Mineral Exploration Geophysicists, Golden CO., 1989, pp. 62-142.
2. Robinson, Lloyd A. et. Al., "Location and Recognition of Discontinuities in Dielectric Media Using Synthetic RF Pulses," *Proceedings of the IEEE*, **62**, No. 1, Jan. 1974.
3. Tomiyasu, Kiyo, "Remote Sensing of the Earth by Microwaves," *Proceedings of the IEEE*, **62**, No. 1, Jan. 1974.
4. Ulaby, Fawwaz T., Moore, Richard K., Fung, Adrian K., *Microwave Remote Sensing Active and Passive*, VOL. 3, Artech House, 1986.
5. Bober, Kenneth M., "Tailoring the Microwave Permittivity and Permeability of Composite Materials," PhD Thesis, University of Massachusetts Lowell, 1993.
6. Sinclair, George, "Theory of Models of Electromagnetic Systems," *Proceedings of the Institute of Radio Engineering*, November 1948.
7. Baker-Jarvis, James, "Improved Technique for Determining Complex Permittivity with the Transmission/Reflection Method," *IEEE Trans. On Microwave Theory and Techniques*, **38**, No. 8, August 1990, pp. 1096-1103.
8. Baker-Jarvis, James, "Transmission / Reflection and Short-Circuit Line Permittivity Measurements," *Natl. Inst. Stand. Technol., Tech. Note 1341, 154 pags*, July 1990, pp. 28-43.
9. Baker-Jarvis et. al., "Transmission/Reflection and Short-Circuit Line Methods for Measuring Permittivity and Permeability," *Natl. Inst. Stand. Technol., Tech. Note 1355-R, 236 pages,* December 1993.
10. Nicolson, A. M. and Ross, G. F., "Measurement of the intrinsic properties of materials by time-domain techniques," IEEE Trans. Instrum. Meas., VOL. IM-17, Dec. 1968.
11. Weir, W. W., "Automatic Measurement of Complex Dielectric Constant and Permeability at Microwave Frequencies," *Proceedings of the IEEE*, **62**, No. 1, January 1974.
12. Ghodgaonkar, D. K., V. V. Varadan, and V. K. Varadan, "A Free-Space Method for Measurement of Dielectric Constants and Loss Tangents at Microwave Frequencies," *IEEE Trans. Instrum. Meas.*, **38**, 1989, pp. 789-793.
13. Vanzura, Eric J. et. al., "Intercomparison of Permittivity Measurements Using the Transmission/Reflection Method in 7-mm Coaxial Transmission Lines," *IEEE Trans. On Microwave Theory and Techniques.*, **42**, No. 11, November, 1994.
14. Umari, Maher H., Ghodgaonkar, D. K., "A Free-Space Bistatic Calibration Technique for the Measurement of Parallel and Perpendicular Reflection Coefficients of Planar Samples," *IEEE Trans. Instrum. Meas.*, **40**, No. 1, Feb. 1991, pp. 19.
15. Sequeira, Brian H., "Extracting $\mu_r$ and $\varepsilon_r$ of Solids from One Port Phasor Network Analyzer Measurements," Martin Marietta Laboratories, MML TR 89-83, Sept. 1989.

16. "Measuring the dielectric constant of solids with the HP 8510 network analyzer," Product note no. 8510-3, Hewlett Packard, 1985.
17. Mason, S.J., "Feedback theory-further properties of signal flow graphs," Proceedings of the I.R.E., **41**, September 1953, pp.1144-1156.
18. Mason, S.J., "Feedback theory-further properties of signal flow graphs," Proceedings of the I.R.E., **44**, July 1956, pp. 920-926.
19. Hornbeck, Robert W., *Numerical Methods*, Quantum Publishers, Inc., 1975, pp. 66-69.
20. Byrne, C. L., Fitzgerald, R. M., "Reconstruction from partial imformation with applications to tomography," SIAM J. Appl. Math. 42, 933-940, 1982.
21. Byrne, C. L., Fitzgerald, R. M., Fiddy, M. A., Hall, T. J., and Darling, A. M., "Image restoration and resolution enhancement," J. Opt. Soc. Am. 73, 1481-1487, 1983.
22. Byrne, C. L., Fitzgerald, R. M., "Spectral estimators that extend the maximum entropy and maximum likelihood methods," SIAM J. Appl. Math. 44, 425-442, 1984.
23. Devaney, A. J., "A filtered backpropagation algorithm for diffraction tomography," Ultrason. Imag. 4, 336-350, 1982.
24. Lin, F. C., Fiddy, M. A., "Image estimation from scattered field data," Int. J. Imag. Sys. Technol. 2, 76-95, 1990.
25. Morris, J. B., Fiddy, M. A., Pommet, D. A., "Nonlinear filtering applied to single-view backpropagated images of strong scatterers," J. Opt. Soc. Am. A 13, 1506-1515, 1996.
26. Giles, Robert H., Gatesman, A.J., Fitz-Gerald, J., Fisk, S. and Waldman, J. "Tailoring Artificial Dielectric Materials at Terahertz Frequencies", The Fourth International Symposium on Space Terahertz Technology , April 1993, Los Angeles, CA.
27. Kekis, John D., Detecting 1/10$^{th}$ Scaled Structures in Dielectric Media Using Monostatic X-Band Radar Scattering Measurements, Masters Thesis, University of Massachusetts Lowell, Dept. of Physics, July, 2000.

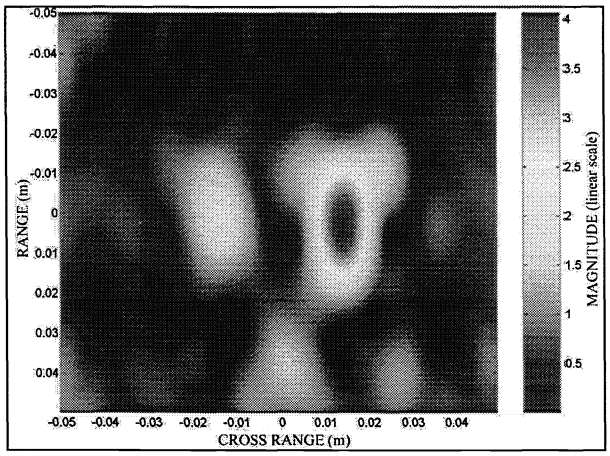


**Figure 3:** Dry ground plane image subtraction (M2-M1); Brass Sphere (d = 0.375") on left, Brass 0.625" Sphere on Right; 0.029m apart.

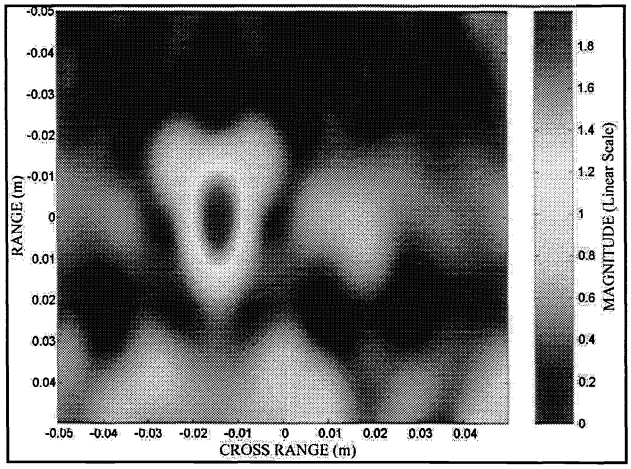


**Figure 4:** Dry ground plane image subtraction (M3-M1); 0.375" sphere on left, VS-50 Mine on right; 0.033m apart.

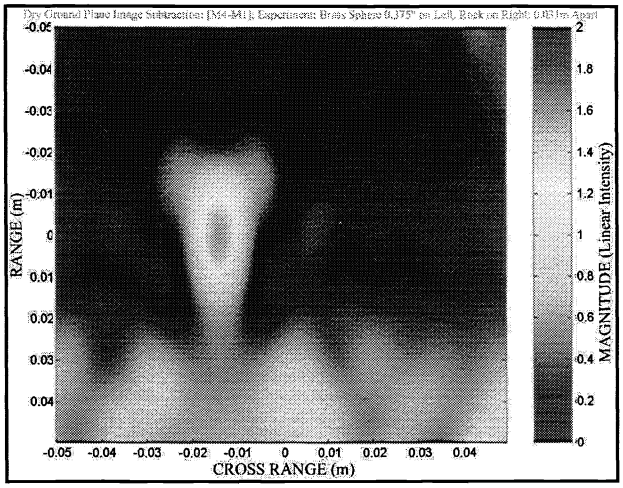


**Figure 5:** Dry ground plane image subtraction (M4-M1); 0.375" Brass sphere on left, Rock on right; 0.0315" apart. Rock is not visible without more superresolution, see Fig 6.

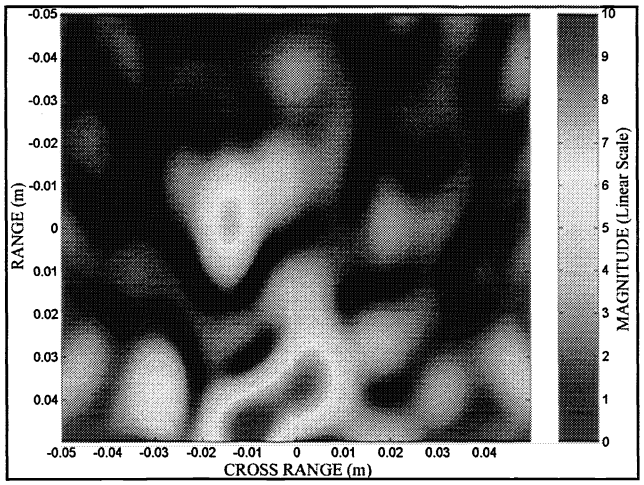


**Figure 6:** Dry ground plane image subtraction (M4-M1); 0.375" Brass sphere on left, Rock on right; 0.0315" apart. Scale is inconsistent from Figures 1 and 2 due to extra superresolution used.

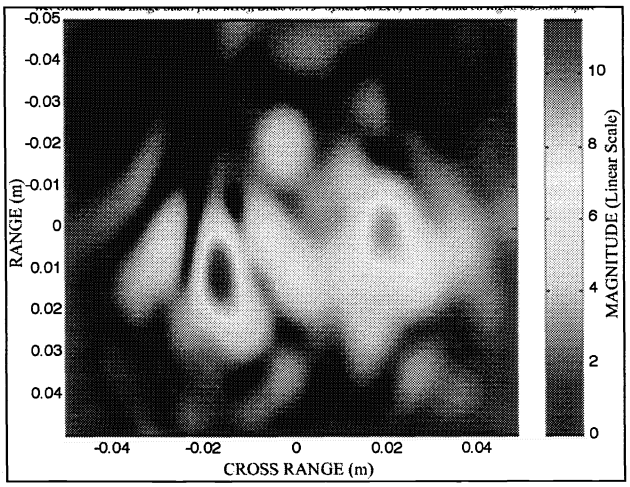


**Figure 7:** Wet ground plane image subtraction (M8-M10); 0.375" Brass sphere on left, VS-50 Mine on right; 0.0315m apart. Scale is inconsistent from Figures 1 and 2 due to extra superresolution used.

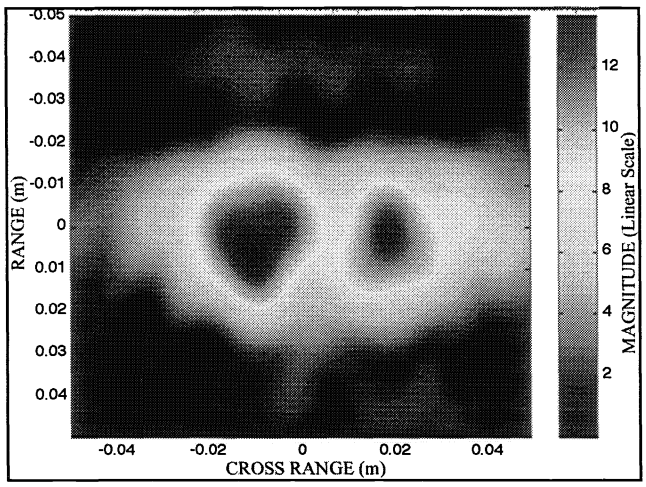


**Figure 8:** Wet ground plane image subtraction (M9-M10); Two VS-50 mines; 0.038m apart. Scale is inconsistent from other images due to extra superresolution used.